Journal of Structural Geology 31 (2009) 1145–1160

Contents lists available at ScienceDirect

Journal of Structural Geology

journal homepage: www.elsevier.com/locate/jsg

Horizontal strain-rates and throw-rates across breached relay zones, central Italy: Implications for the preservation of throw deficits at points of normal fault linkage

J.P. Faure Walker [a,*], G.P. Roberts [a], P.A. Cowie [b], I.D. Papanikolaou [a], P.R. Sammonds [a], A.M. Michetti [c], R.J. Phillips [b]

[a] Research School of Earth Sciences, UCL/Birkbeck, Gower Street, London, WC1E 6BT, UK
[b] Institute of Geography School of GeoSciences, University of Edinburgh, Drummond Street, Edinburgh, EH8 9XP, UK
[c] Universita dell'Insubria, Dipartimento di Scienze, CC.FF.MM., Via Lucini, 3, 22100, Como, Italy

ARTICLE INFO

Article history:
Received 20 December 2008
Received in revised form
6 June 2009
Accepted 11 June 2009
Available online 21 June 2009

Keywords:
Active normal fault
Relay ramp
Breaching
Kostrov strain
Rates of breaching

ABSTRACT

In order to investigate the relationship between the throws and 3D orientation of breaching faults crossing relay zones, kinematic data, throw-rates and total throws have been measured for an active normal fault in the Italian Apennines that displays a relay zone at its centre. The c. 0.8 km long breaching fault dips at 67 ± 5° and strikes obliquely to c. 2–3 km long faults outside the relay zone which dip at 61 ± 5°. Total throws of pre-rift limestone define a throw profile with a double maximum (370 ± 50 m; 360 ± 50 m) separated by an area of lower throw (100 ± 50 m) where the breaching fault is growing. Throw-rates implied by offsets across bedrock scarps of Late Pleistocene–Holocene landforms (15 ± 3 ka) are higher across the breaching fault (0.67 ± 0.13 mm/yr) than for locations of throw maxima on the neighbouring faults (0.38 ± 0.07 mm/yr; 0.55 ± 0.11 mm/yr). The deficit in total throw will be removed in 0.68–1.0 Myr if these deformation rates continue. To investigate why the highest throw-rates occur in the location with lowest total throw, Kostrov horizontal strain-rate tensors were calculated in 1 × 2 km boxes. We show that the oblique strike and relatively high dip of the breaching fault mean that it must have a relatively high throw-rate in order for it to have a horizontal strain-rate concomitant with its position at the centre of the overall fault. We show that whether throw minima at locations of fault linkage are preserved during progressive fault slip depends on the 3D orientation of the breaching fault. We use the above to discuss the longevity of throw deficits and multiple throw maxima along faults in relation to seismic hazard and landscape evolution.

1. Introduction

Displacement-rates on active faults control seismic hazards (Main, 1996; Nicol et al., 1997; Walsh et al., 2003a; Roberts et al., 2004; Bull et al., 2006) and provide a timescale with which to assess the mechanisms operating during continental deformation (e.g. Cowie et al., 2005). Knowledge of displacement-rates on the largest faults within extensional basins, and throw-rates if there is no information on fault dip, is improving due to outcrop and seismic reflection studies, numerical simulations and insights from scaling relationships (Dawers and Anders, 1995; Cowie, 1998; McLeod et al., 2000; Cowie and Roberts, 2001; Roberts and Michetti, 2004). However displacement-rate or throw-rate histories within zones of fault linkage (i.e., breached relay zones) are less well characterised and it is common for deficits in displacement or throw to exist in those locations (Bull et al., 2006; Jackson et al., 2002; Walsh et al., 2003a). On a newly linked fault, displacement will be greater either side of the breached relay zone resulting in a profile that has two displacement maxima (e.g. Jackson et al., 2002). This double maxima with a displacement deficit in the former relay zone after linkage forms due to the fact that this location has experienced faulting for a shorter period of time than locations along the two neighbouring faults.

The key question that arises is whether (a) the throw deficit persists during subsequent slip because the newly linked fault has no memory of the mechanical discontinuity at the point of linkage (Walsh et al., 1996); this would explain why many throw profiles show multiple maxima separated by minima at zones of former linkage (McLeod et al., 2000, for example), or (b) the point of linkage develops high throw-rates that work to remove the throw

* Corresponding author. Tel.: +44 773 496 6032.
E-mail address: j.faure-walker@ucl.ac.uk (J.P. Faure Walker).

0191-8141/$ – see front matter © 2009 Elsevier Ltd. All rights reserved.
doi:10.1016/j.jsg.2009.06.011

deficit (Gupta and Scholz, 2000). Fig. 1 shows these possible scenarios. By investigating how the 3D orientation of a fault affects the strain-rate across it, we suggest that whether the throw deficit persists is dependent on the 3D orientation of the breach fault relative to the outer faults.

There is extensive literature on relay zones and breaching faults (e.g. Peacock and Sanderson, 1991; Walsh et al., 1999; Peacock, 2003). This work has studied displacement gradients on the bounding faults, rotation of the bedding in the relay ramp, strain in the relay ramp due to fracturing, throw deficits across the relay zone, and the overlap, overstep and linkage of the bounding faults. However, there is little information on the dips of breaching faults and how the kinematics and 3D geometry of the faults change across a breached relay zone (cf. Walsh et al., 2003b). This paper demonstrates why these observations are critical in the evolution of throw profiles across the breached relay zone.

The normal fault we study in central Italy has a relay zone at its centre that is undergoing breaching (Fig. 2). A fault is growing within the relay zone with an orientation oblique to that of the faults either side of the relay zone. The breach fault is not connected to the adjacent faults at the surface. Excellent exposure allows measurements to be made of (1) the total throw across the faults, (2) rates of throw accumulation revealed by offsets of a 15 ± 3 kyr geomorphic surface, (3) the kinematics of the faulting revealed by striated and corrugated fault planes, and (4) the dips and strikes of the faults (Figs. 3 and 4). The throw-rate over the last 15 ± 3 kyr is significantly higher across the breach fault than along the two neighbouring faults along strike, while the total throw is less across the breach fault. If the throw-rates are representative of longer time periods (see Bull et al. (2006) and Nicol et al. (2006) who show that displacement-rates stabilise over time periods greater than 8 kyr and less than 18 kyr), these two pieces of information suggest the breach fault is younger (Fig. 5a). This suggests a deficit in total throw at the point of linkage is being removed by the relatively high rates of throw accumulation. We emphasise through calculation of horizontal strain-rates using a modification of the Kostrov equations (Kostrov, 1974) that a fault that has a slip vector which is oblique to fault strike (non dip-slip) has a lower principal horizontal strain-rate than a fault with pure dip-slip motion with the same length, throw and dip (Fig. 6). Thus, in order to maintain the highest principal horizontal strain-rate at the centre of a newly linked fault where an oblique breach fault has formed, a relatively high throw-rate is needed. The dip of the breach fault relative to the outer faults will also affect the strain-rate: the steeper the breach fault, the higher the throw-rate required to maintain a uniform horizontal strain-rate (Fig. 7). This relatively high throw-rate works to remove the throw deficit. In the example we study, we suggest that relatively high throw-rates have developed within the relay zone (1) because the breach fault is in the centre of the fault system where the highest deformation rates are to be expected and (2) because of its oblique strike and relatively high dip within the strain-rate field defined by the kinematics and rates of faulting.

We use this information to discuss strain-rate accumulation in other examples of relay zones that have undergone linkage, and what this implies for our understanding of seismic hazards related to fault throw-rates and landscape evolution.

2. Geological background and deformation rate data

The Apennines, Italy, is a region of extending continental crust positioned within the zone of convergence between the Eurasian and African Plates (Anderson and Jackson, 1987; Doglioni, 1993; Jolivet et al., 1998) (Fig. 2). Northward motion of the African plate through the late Mesozoic–Recent has led to subduction of Tethyan ocean crust and collision of fragments of continental crust which now form the northern margins of the Mediterranean Sea. Thrusting continues to the present day on the Adriatic side of the Apennines, but in general, NE-directed thrusting in the inner part of central Italy ceased in the Pliocene (Patacca et al., 1990). Subsequently, SW-NE extension began, with rocks as old as at least c. 2.5 Ma infilling extensional basins in the Lazio-Abruzzo Apennines (Cavinato et al., 2002). Major active normal faults are 20–40 km in length, with total throws of <c. 2 km (Roberts and Michetti, 2004). The hanging-walls of the faults are marked by Plio-Quaternary continental basins. The faults exhibit converging patterns of fault slip that are known to typify faults in the

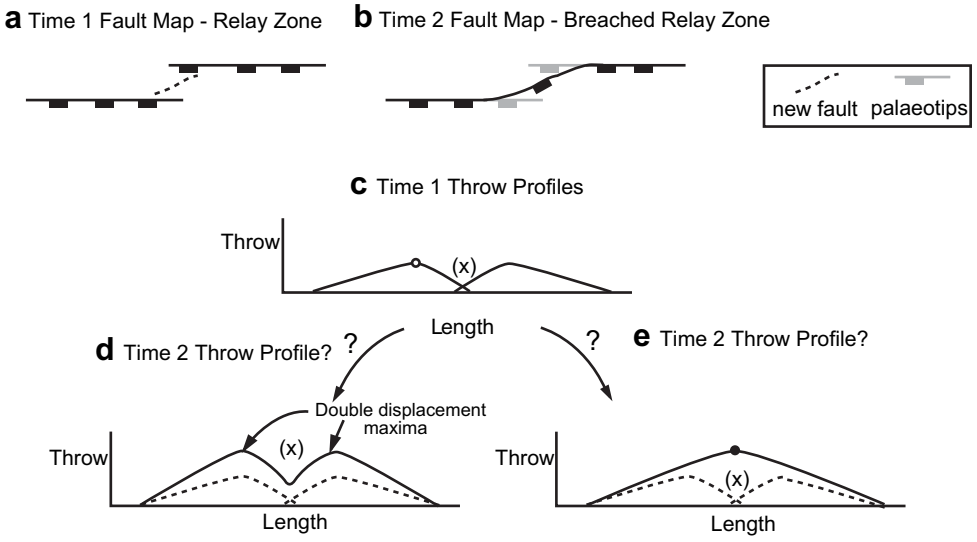

Fig. 1. Cartoon (a)–(e) showing possible scenarios for the evolution of throw across a relay zone between two normal faults where a breaching fault (x) develops. (c) The throw profile across the fault zone when the breach fault initiates, as shown in map view in (a). Once the breach fault develops (b), the throw profile may develop with time to case (d) or (e). These differ due to the existence of a double throw maxima in (d), contrasting with a single throw maxima at the point of linkage in (e). In (d) the rate of throw accumulation is relatively uniform along strike (e.g. McLeod et al., 2000), whereas in (e) throw-rates within the breached relay zone increase in the zone of total throw deficit to restore a single throw maxima.

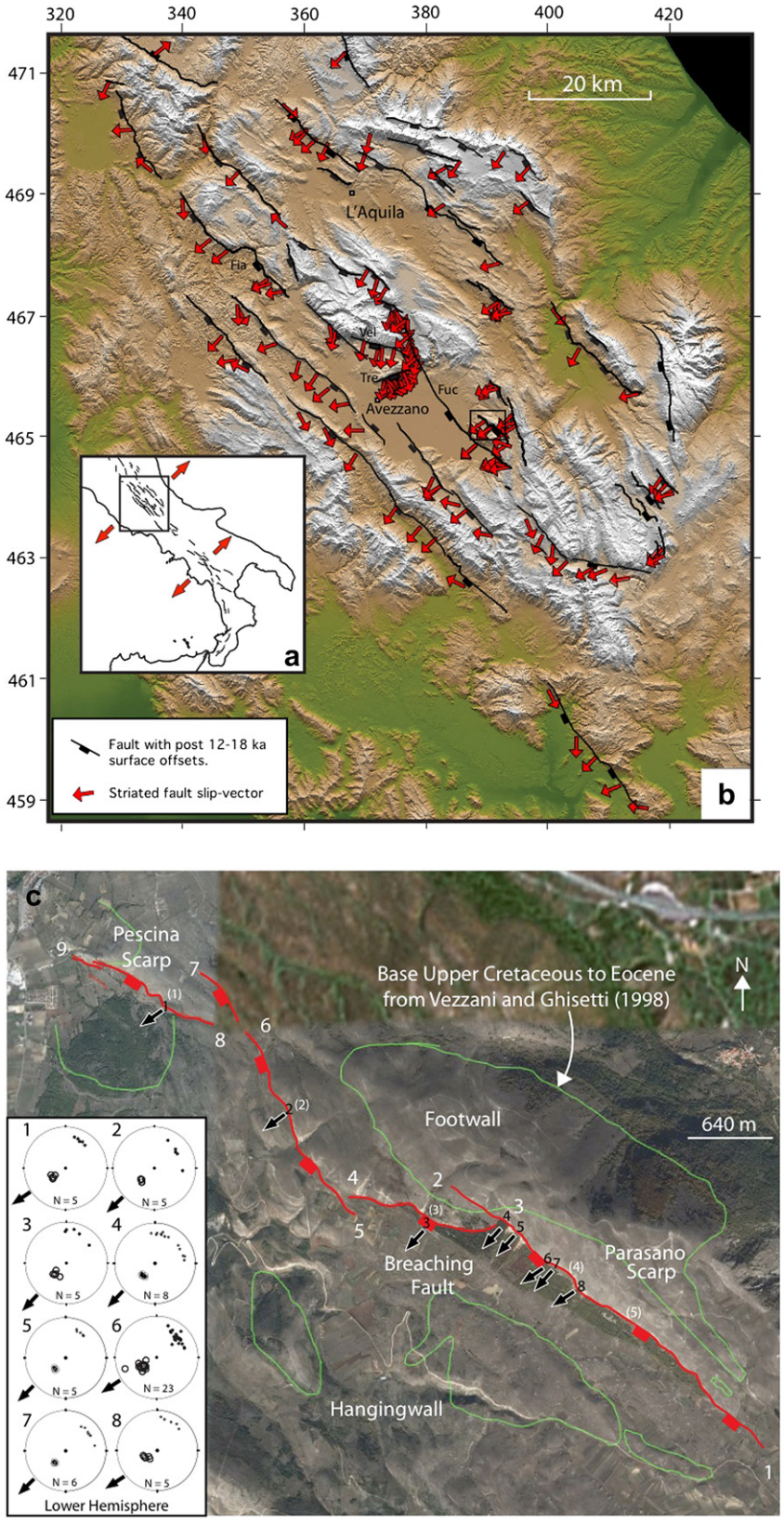

Fig. 2. Map and overhead imagery locating the Pescina–Parasano fault scarps within the zone of extension within the central Apennines, Italy. Imagery from Google Earth™. Kinematic data are from the main fault planes that are characterised by corrugations and frictional wear striae that indicate the fault-slip direction. Arrows show the fault-slip direction measured at that point and the black numbers show which stereonets the arrows correspond to. The fault traces, topography and fault throws define a relay ramp that contains a fault that is attempting to breach the relay and link the two neighbouring faults. The white numbers without brackets identify fault tips discussed in the text. The white numbers in brackets show the locations of the scarp profiles shown in Fig. 4. The base of the Upper Cretaceous to Eocene limestone formation is from Vezzani and Ghisetti (1998). Vel, Velino fault; Tre, Tre Monti fault; Fuc, Fucino fault; Fia, Fiamignano fault.

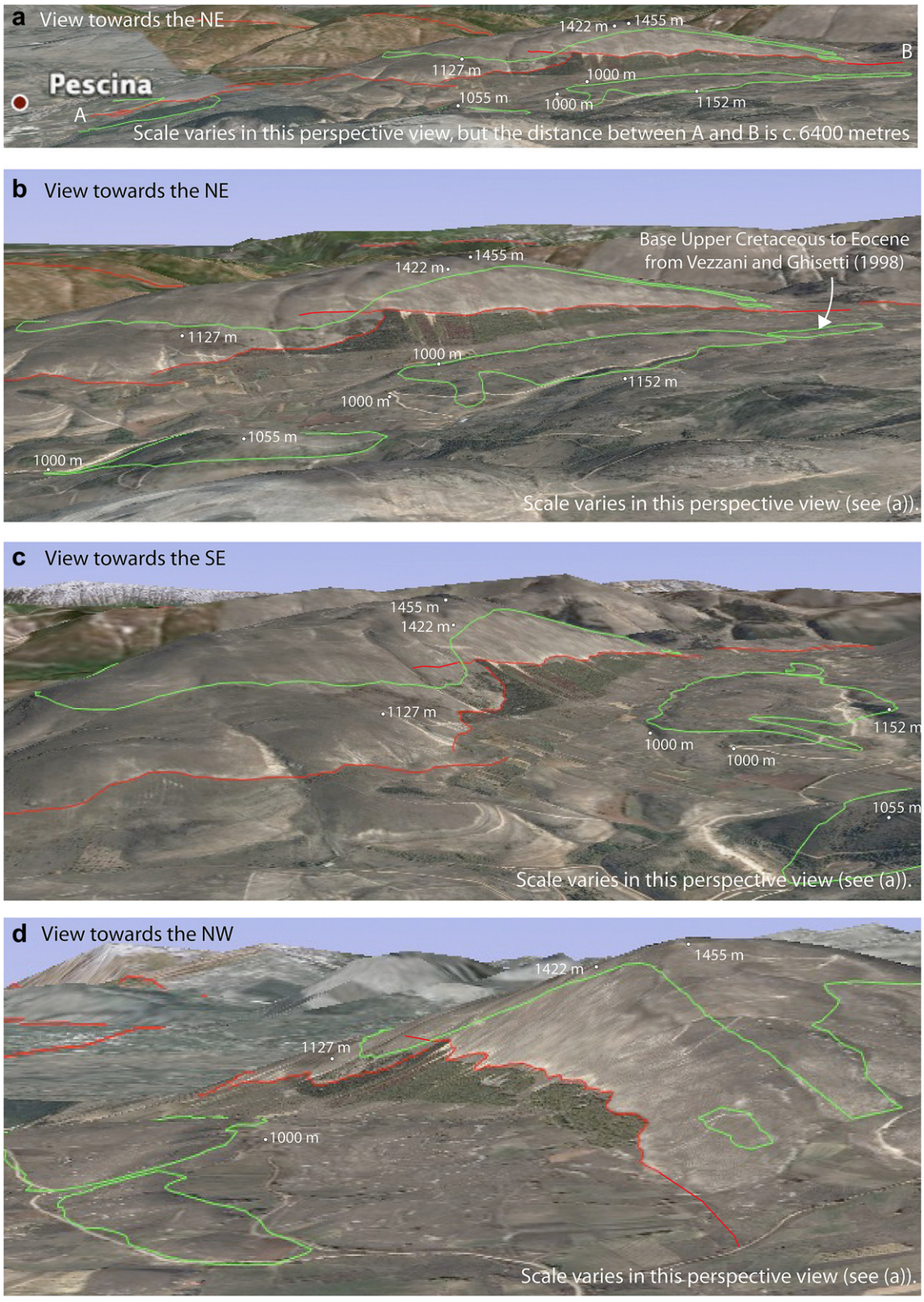

Fig. 3. 3D views of the topography, fault geometries and elevations of the base of the Upper Cretaceous to Eocene. Imagery from Google Earth™. Base Upper Cretaceous to Eocene from Vezzani and Ghisetti (1998). Elevations from Vezzani and Ghisetti (1998) and barometric altimetry.

Apennines (Roberts and Michetti, 2004). These converging slip vectors combine to accommodate SW-NE extension. Slip-rates on the active normal faults in the central Apennines can be determined from offsets of deposits and landforms dating from the last glacial maximum (12–18 ka) (Roberts and Michetti, 2004). Smooth hillsides, that are typical of former periglacial processes, are offset by bedrock fault scarps. The footwalls of the scarps are formed of Mesozoic and Tertiary limestones, whilst the hanging-walls are

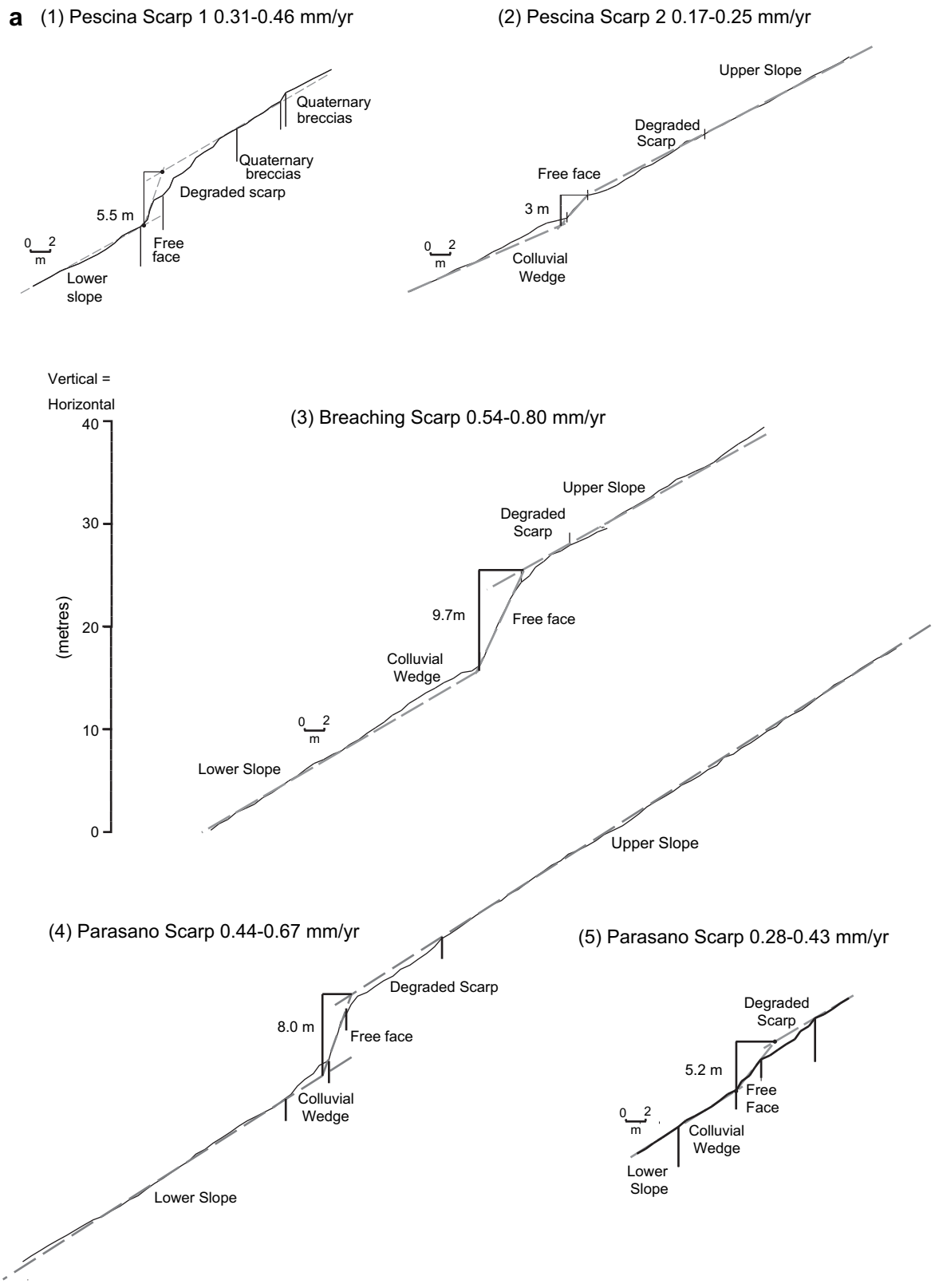

Fig. 4. (a) Topographic profiles across fault scarps offsetting 12–18 ka slopes. Location numbers for profiles are located on Figs. 2a and 5. (b) Photographs of scarp profile sites and a view of the fault scarp from a distance.

marked at the surface by the accumulations of Pleistocene colluvium that, at faulted outcrops, date mainly from the last glacial maximum. The colluvial hanging-wall surfaces and the smooth slopes of limestone in the footwall are covered by a few tens of centimetres of organic-rich soil which also contains tephra erupted from the volcanic province of the western, Tyrrhenian coast of Italy. An extensive database of radiocarbon dates and tephrachronology show that the smooth hillsides date from the last

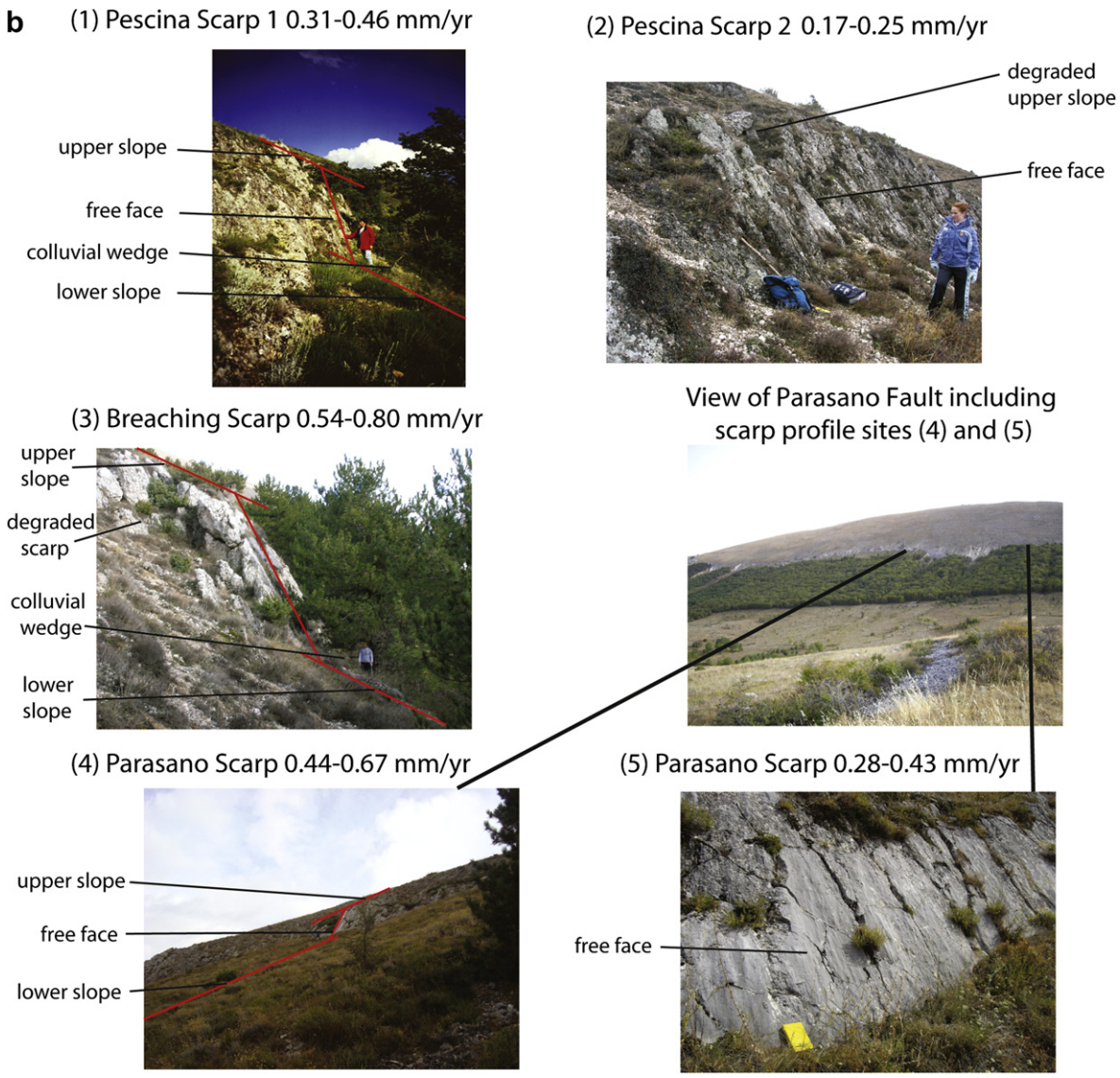

Fig. 4. (*continued*).

glacial maximum (12–18 ka) (Giraudi and Frezzotti, 1997; Roberts and Michetti, 2004). The 12–18 ka age of the scarps is also confirmed by ^{36}Cl cosmogenic exposure dates for the fault planes exposed along the scarps (see Palumbo et al. (2004) and Roberts (2006) for a discussion of the age). The throws associated with scarps that offset these dated slopes is a measure of the throw-rate averaged over the age of the slope. Hence an 18 ka scarp that has a throw of 18 m yields a throw-rate of 1 mm/yr, but a throw-rate of 1.5 mm/yr if the scarp has formed since 12 ka. Published studies of displacement-rates over 10^3–10^4 yr timescales show that slip-rates on active faults stabilise over time periods greater than 8000 yr and less than 18,000 yr (Bull et al., 2006; Nicol et al., 2006) so the rates measured from the offsets of slopes dating from 12 to 18 ka probably represent the long-term rates of slip. We have studied the Parasano-Pescina fault scarps (Fig. 2). These have been described by a number of authors (see Roberts and Michetti (2004) for a review) but they have not given details of the evolution of the relay zone within this system of scarps. These scarps probably ruptured at the surface during the 1915 Fucino earthquake with surface slip of c. 0.5–1.0 m (Ms 6.9; 33,000 fatalities) (Margottini and Screpanti, 1988) although it is not absolutely clear which of the scarps in Fig. 2 ruptured due to a lack of clarity in historical observations of surface ruptures. A Base Upper Cretaceous to Eocene marker horizon is offset across the faults providing values for total throw (Vezzani and Ghisetti, 1998).

3. Method

We have mapped the scarps onto high-resolution overhead images, drawn serial cross-sections across published geological maps to gain the total vertical offsets across the faults, measured the kinematics of the faulting from striated and corrugated fault surfaces, and surveyed the scarps to measure the vertical offsets that have developed since 12–18 ka. We then calculated strain-rate tensors using an adaptation of the methods from Kostrov (1974).

The faults were mapped onto high-resolution overhead images within Google Earth™, that allowed the fault traces to be located within a few metres of their actual positions (Fig. 2). Existing geological mapping reveals how the base of a 150–200 m thick Upper Cretaceous to Eocene limestone has been deformed by the faults (Vezzani and Ghisetti, 1998). Topographic maps plus elevations obtained using barometric altimeters carried in the field revealed the elevations of the base of this limestone and how this changes both along and across the faults. This contact was mapped into Google Earth™, allowing 3D

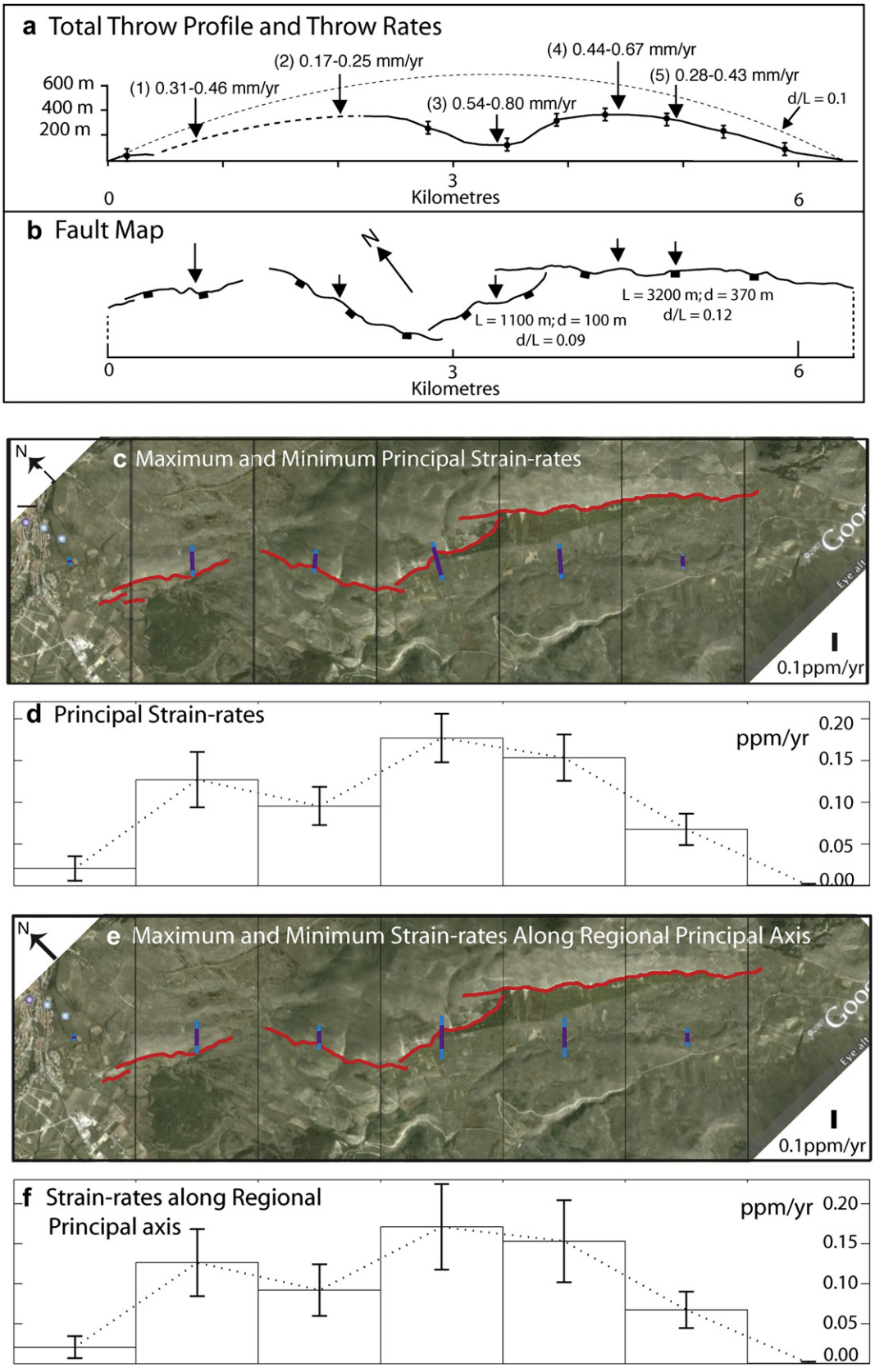

Fig. 5. (a) Throw profiles defined by the elevations of the base of Upper Cretaceous to Eocene limestones around the Parasano–Pescina fault scarps. Throw-rates derived from the scarp profiles in Fig. 4 are indicated as are d/L ratios for the faults (where certain) and for the overall system if the faults link. The highest throw-rates occur where there is a deficit in total throw within the incipient breached relay ramp. (b) Fault map. (c) Principal strain-rates calculated over 15 ± 3 ka within 1×2 km grid boxes orientated with axes NW-SE and NE-SW; blue, maximum; purple, minimum. (d) Graph of principal strain-rates showing the average principal strain-rates shown in (c). (e) Map and (f) graph of strain-rates along the principal axis of the entire fault (approx SW-NE) within 1×2 km grid boxes orientated with axes NW-SE and NE-SW.

perspective views of the deformation to be gained (Fig. 3); this vertical offset of the limestone includes any bed rotation within the relay zone (Walsh et al., 1996). We extrapolated the elevations of this contact onto the fault during cross-section construction, assuming little or no folding in the vicinity of the fault. Roberts and Michetti (2004) show that there is little or no folding of beds in the vicinity of a well-exposed normal fault in the Apennines (Fig. 5 of Roberts and Michetti, 2004), implying that strains related to folding do not alter our conclusions. The kinematics of 8 locations along the faults were measured from striated and corrugated fault planes and this revealed that the deformation involved mainly dip-slip normal faulting towards the southwest (Fig. 2). We then constructed detailed topographic profiles (Fig. 4) across the faults using a 1 m rule and clinometer that we checked with barometric altimeters and field photographs with clear scales (Fig. 4). These topographic profiles reveal the vertical offsets of the 12–18 ka surface that formed during the high erosion and sedimentation rates that characterised the last glacial maximum in the Apennines. In particular, we took special care to identify the upper slope, degraded scarp, free face of the scarp (fault plane), colluvial wedge, and the lower slope (Fig. 8); these features are known to be the key features that need to be constrained to characterise Holocene vertical offsets across active normal fault scarps (see Papanikolaou et al. (2005) for a review). The above allowed determination of the lengths, total throws, throw-gradients, and throw-rates for the faults.

We use the measured throw-rates and slip direction data to calculate strain-rate tensors using techniques adapted from Kostrov (1974) and following the lead of other workers (Holt and Haines, 1995; England and Molnar, 1997) we express the strain-rate tensor in terms of components that can be measured at outcrop; we explain this method below. A detailed explanation of our method for calculating strain-rates can be found in Faure Walker et al. (submitted for publication).

Kostrov (1974) demonstrated that, if all the strain in a volume is seismic and the dimensions of the faults are small relative to the region, the average strain tensor, $\bar{\varepsilon}_{ij}$, within the volume can be obtained by summing the moment tensors of all the earthquakes occurring along faults within it:

$$\bar{\varepsilon}_{ij} = \frac{1}{2\mu V}\sum_{k=1}^{K} M_{ij}^{k} \tag{3.0.1}$$

where $\bar{\varepsilon}_{ij}$ represents the ith component of strain acting on the plane normal to the jth axis, M_{ij}^{k} is the ijth component of the moment tensor of the kth earthquake occurring within a volume V, K is the total number of earthquakes and μ is the shear modulus.

If the region has dimensions smaller than the length of the faults the strain-rate is calculated by summing the moment rate released on the length of each fault segment within the volume (Molnar, 1983) and can be expressed in terms of parameters that can be measured in the field, without *a priori* knowledge of the thickness of the seismogenic layer or the shear modulus in the region (England and Molnar, 1997).

A flat earth approximation is used for the region considered as it only spans less than a degree latitude and longitude; the curvature of the earth becomes important when the region considered covers more than 10–15° (Haines and Holt, 1993).

The horizontal component of the strain-rate tensor along the axes co-planar and perpendicular to the direction the strike of the plane and slip direction are being measured from, expressed in terms which can be measured in the field (see Fig. 8), is:

$$\dot{\bar{\varepsilon}}_{11} = \frac{1}{at}\sum_{k=1}^{K} L^{k}T^{k}\cot p^{k}\sin\phi^{k}\cos\Phi^{k} \tag{3.0.2}$$

where Φ is the strike, ϕ is the slip direction, p is the plunge, T is the throw of a given fault in time, t, on a fault k, K is the number of faults within the surface area of the region concerned, a, and L^{k} is the length of the fault segment contained within the area.

Using results derived in Fung (1977), the strain-rate tensors can be expressed in terms of the principal strain-rate along the horizontal principal axis, which is the direction of maximum strain-rate within the horizontal plane.

The principal horizontal strain-rate, expressed in terms which can be measured in the field, is given by:

$$\dot{\bar{\varepsilon}}_{1'1'} = \frac{1}{2at}\sum_{k=1}^{K}\left\{L^{k}T^{k}\cot p^{k}\left[\sin(\phi^{k}-\Phi^{k})+\sin\left(\phi^{k}+\Phi^{k}+\arctan\left(\frac{\sum_{k=1}^{K}L^{k}T^{k}\cot p^{k}\cos(\phi^{k}+\Phi^{k})}{\sum_{k=1}^{K}L^{k}T^{k}\cot p^{k}\sin(\phi^{k}+\Phi^{k})}\right)\right)\right]\right\} \tag{3.0.3}$$

The principal angle, θ, is measured counter-clockwise between the "1" coordinate axis of the measured strain-rate tensor and the principal horizontal axis direction:

$$\theta = \frac{1}{2}\arctan\left(\frac{\sum_{k=1}^{K}L^{k}T^{k}\cot p^{k}\cos(\phi^{k}+\Phi^{k})}{\sum_{k=1}^{K}L^{k}T^{k}\cot p^{k}\sin(\phi^{k}+\Phi^{k})}\right) \tag{3.0.4}$$

ψ is the principal angle measured clockwise from north (i.e. $\psi = 90-\theta$).

Eqs. (3.0.2) and (3.0.3) are used in this paper to calculate the horizontal components of the average strain-rate tensor along the regional extension direction (northeast-southwest) and in the horizontal principal directions within volumes with 1 km × 2 km surface areas on a Universal Transverse Mercator (UTM) map projection within the Italian Apennines. The rectangles were arranged with their edges aligned along NW-SE and NE-SW axes parallel and perpendicular to the average orientation of the faults. Throw-rate and slip direction data are interpreted linearly between locations where data have been collected and where the faults cross grid lines. At the ends of the faults where throws across scarps decrease to zero, the 12–18 ka throw is assigned as zero; the slip direction and plunge at the tips are assigned the values measured closest to the tips.

Implicit to this method is the assumption that all the faults in the region are known. The 15 kyr strain-rates measured in this paper only include faults exposed at the surface, so we do not record strains from earthquakes below the threshold for surface slip, which is about Ms 5.5–6.0 in the Apennines (Michetti et al., 2000).

3.1. Strain-rates within areas containing one fault segment

To aid our interpretation of the natural example in the Apennines, we use the equation for the principal strain, Eq. (3.0.3), to calculate strain-rate values for a hypothetical area containing only one fault segment; in this case:

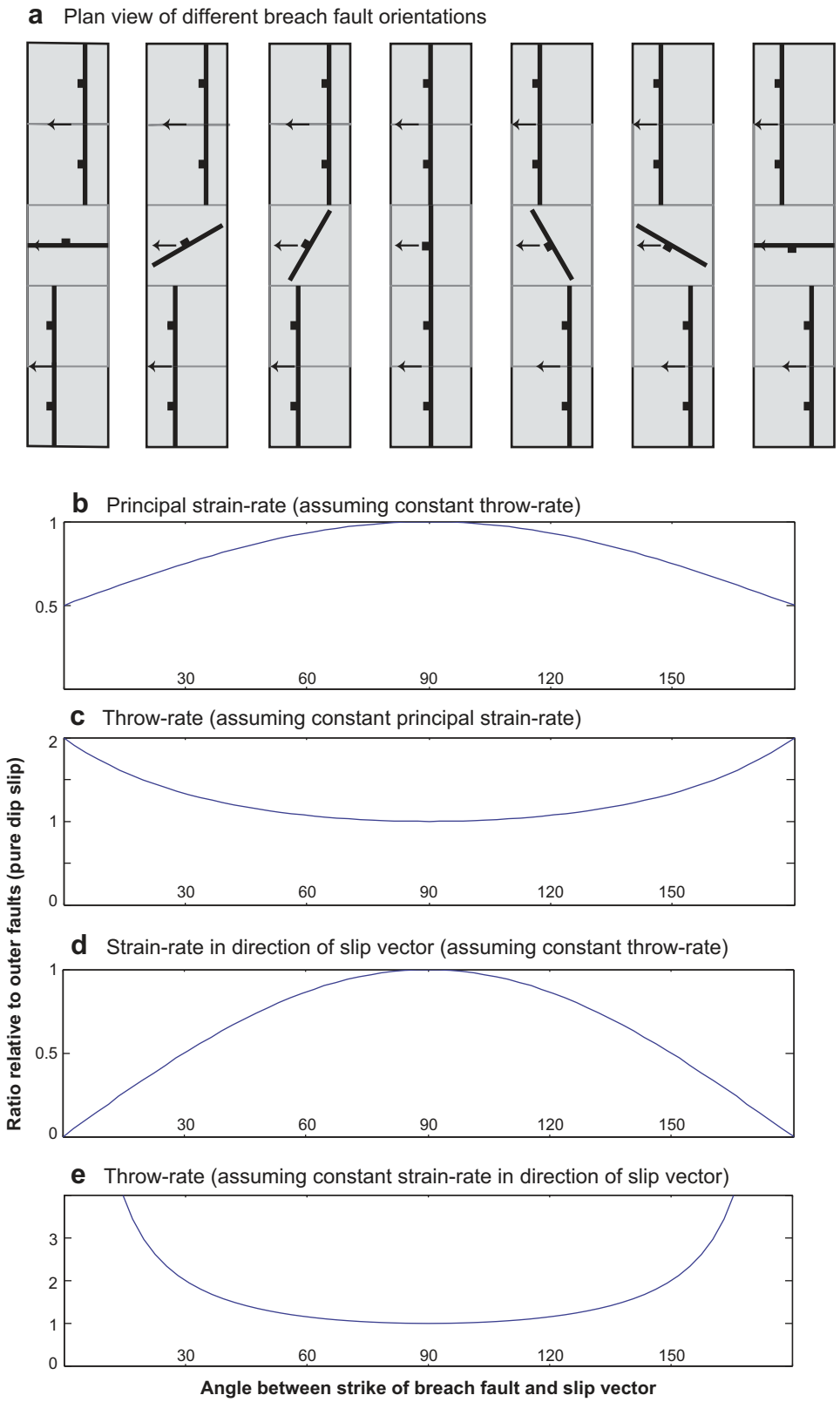

Fig. 6. (a) Cartoon showing example orientations of a breach fault with constant slip vector and length equal to adjacent fault lengths within grid boxes. (b)–(e) Graphs showing how the orientation of the breach fault affects the strain-rate and throw-rate expressed as a ratio relative to adjacent outer faults (pure dip-slip) against angle between the slip vector and the strike of the fault, assuming constant length, slip vector (plunge and trend) and grid area. (b) Principal strain-rate magnitude assuming a constant throw. (c) Throw-rate assuming a constant principal strain-rate magnitude. (d) Axis strain-rate (in the direction of the slip vector) assuming a constant throw-rate. (e) Throw-rate assuming a constant axis strain-rate.

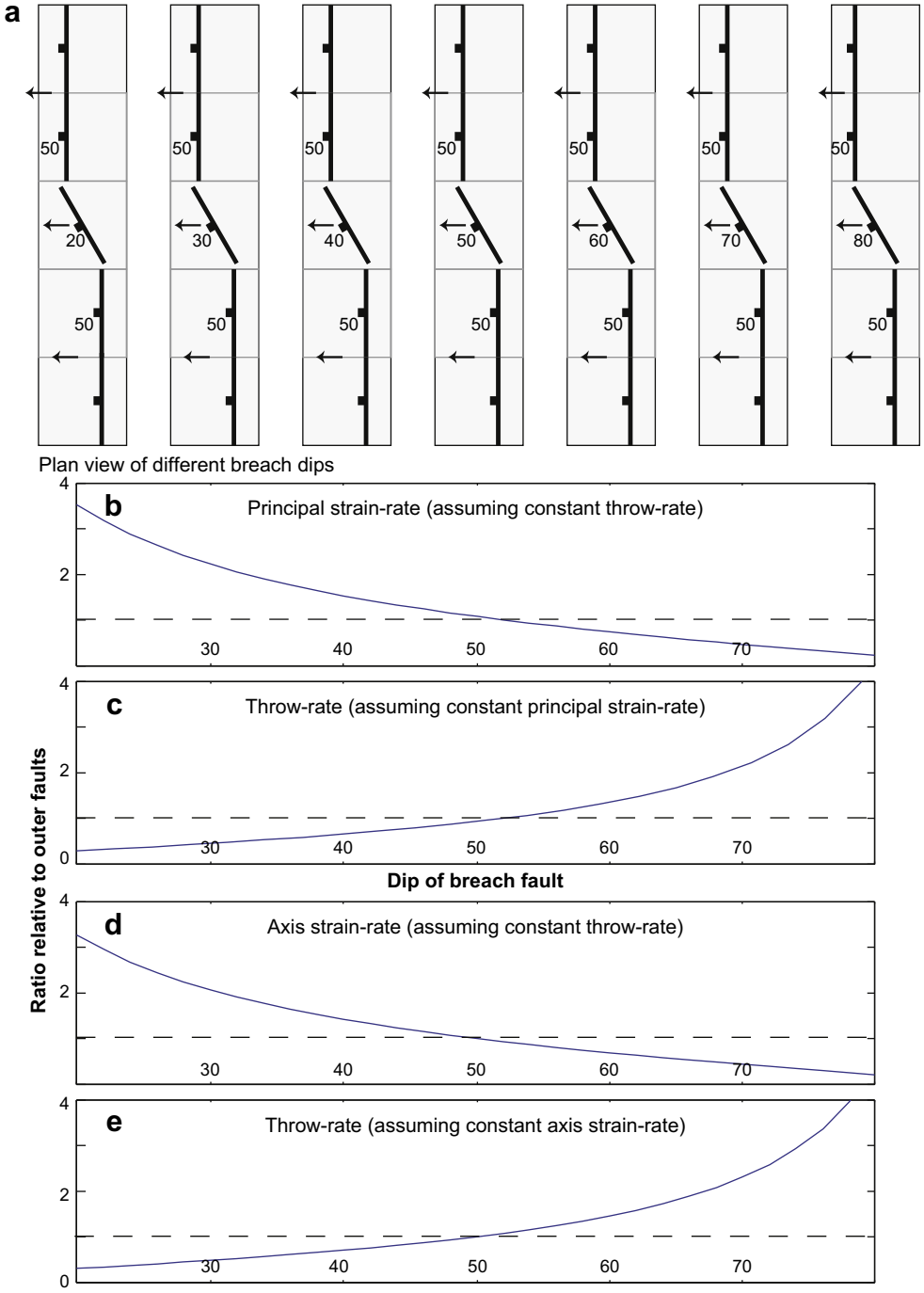

Fig. 7. (a) Cartoon showing example dips of an oblique breach fault with constant slip vector azimuth and length equal to adjacent fault lengths within grid boxes. (b)–(e) Graphs showing how the dip of the breach fault affects the strain-rate and throw-rate expressed as a ratio relative to adjacent outer faults against dip angle of the fault, assuming constant length, slip vector azimuth and grid area. (b) Principal strain-rate magnitude assuming a constant throw-rate. (c) Throw-rate assuming a constant principal strain-rate magnitude. (d) Axis strain-rate (in the direction of the slip vector) assuming a constant throw-rate. (e) Throw-rate assuming a constant axis strain-rate.

$$\dot{\varepsilon}'_{1'1'} = \frac{LT\cot p}{2at}[\sin(\phi-\Phi)+\sin(\phi+\Phi+\arctan(\cot(\phi+\Phi)))] = \frac{LT\cot p}{2at}[\sin(\phi-\Phi)+1] \quad (3.1.1)$$

$$\dot{\varepsilon}_{11} = \frac{1}{at}LT\cot p\sin\phi\cos\Phi \quad (3.1.2)$$

Eq. (3.0.2) for the strain-rate along the "1"-direction (direction approximately perpendicular to the strike of the fault system) simplified for an area containing only one fault segment is:

Eqs. (3.1.1) and (3.1.2) show that fault orientation, slip vector, throw-rate and strain-rate are inter-dependent. Two specific examples of breach fault variations are described in Sections 3.1.1 and 3.1.2.

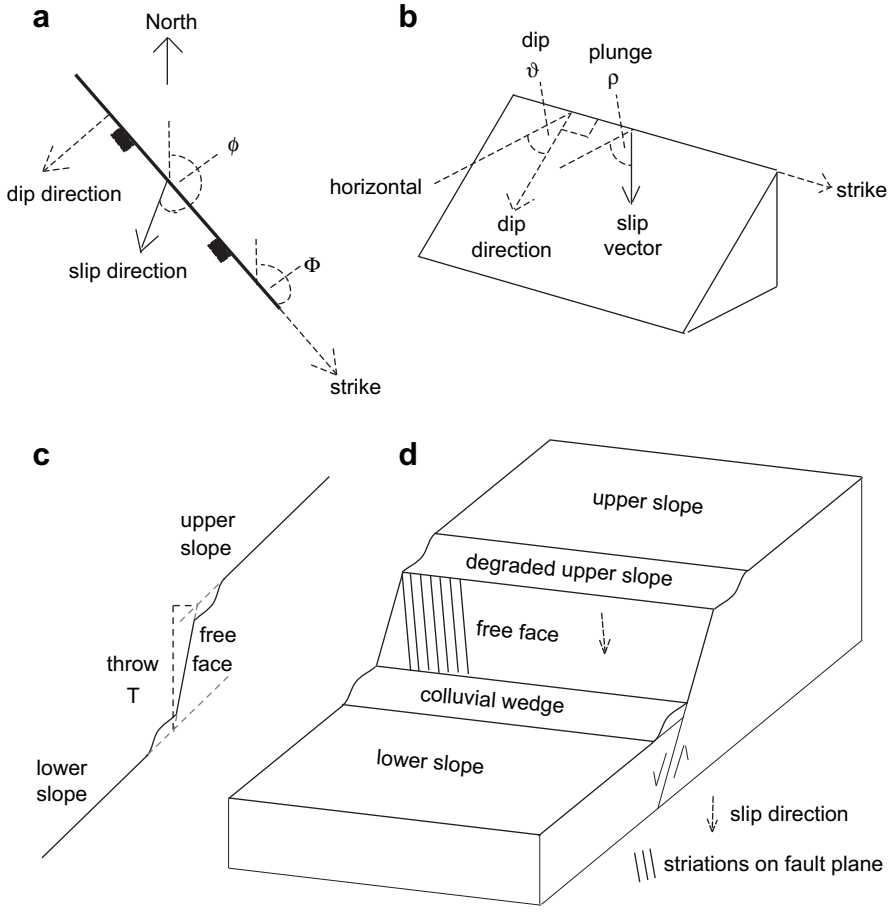

Fig. 8. Schematic diagrams showing measurements taken in the field and symbols used in strain calculations. (a) Map view of fault, (b) view of fault plane, (c) cross-section of throw profile construction and (d) cartoon of slope offset estimated using profile in (c).

3.1.1. Scenario a: Breach fault has same slip vector as outer fault (Fig. 6)

Eq. (3.1.1) shows that, for a given fault length, if the slip vector azimuth and plunge remain constant across the relay zone, then within same-sized grid boxes:

$$\dot{\bar{\varepsilon}}'_{1'1'} \propto T[\sin(\phi - \Phi) + 1] \tag{3.1.3}$$

Thus, in order to have the same principal strain-rate in different grid boxes:

$$T \propto \frac{1}{[\sin(\phi - \Phi) + 1]} \tag{3.1.4}$$

The above relationship implies that in order to maintain constant principal strain-rates across a breach fault, the throw-rate will increase as the strike becomes more oblique, that is, it varies from a pure dip-slip scenario to having a greater strike-slip component of slip.

Eq. (3.1.2) shows that if the length and slip vector remain constant, then within same-sized grid boxes:

$$\dot{\bar{\varepsilon}}_{11} \propto T\cos\Phi \tag{3.1.5}$$

Therefore, in order to have the same strain-rate along the 1-axis the throw will increase as the fault obliquity increases:

$$T \propto \frac{1}{\cos\Phi} \tag{3.1.6}$$

Fig. 6 shows the relationships between fault orientation, throw-rate and strain-rate graphically as ratios relative to the case in which the slip direction is normal to the strike of the fault (pure dip-slip).

Note that the dip, plunge, slip vector and strike are related by the equation:

$$\tan p = \tan\vartheta \sin(\phi - \Phi) \tag{3.1.7}$$

Thus, if the plunge and azimuth of the slip vector remain constant, the dip of the fault will increase as the angle between the slip vector and strike decreases, that is, as the fault becomes more oblique.

Note the same inferences would be reached if the strike were kept constant and the slip vector trend varied as it is the angle between them that affects the principal horizontal strain-rate.

3.1.2. Scenario b: Breach fault has same strike and slip vector azimuth as outer faults (Fig. 7)

If the fault length, strike and slip vector azimuth remain constant, using Eqs. (3.1.1), (3.1.7) and (3.1.2), it can be shown that the principal horizontal strain-rate and strain-rate in the direction of the slip vector increase as the dip decreases:

$$\dot{\bar{\varepsilon}}'_{1'1'} \propto \frac{T\cot\vartheta}{\sin(\phi - \Phi)}[\sin(\phi - \Phi) + 1] \propto T\cot\vartheta \tag{3.1.8}$$

$$\dot{\bar{\varepsilon}}_{11} \propto T\frac{\cot\vartheta}{\sin(\phi - \Phi)} \propto \cot\vartheta \tag{3.1.9}$$

a 3D views of a relay zone before and after breaching

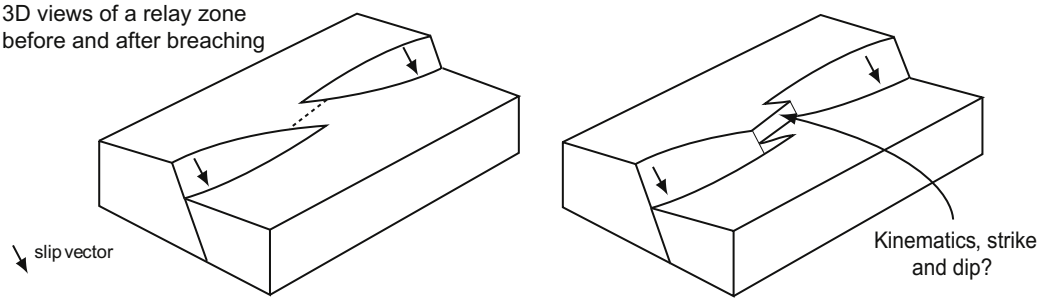

b Graph showing how the dip of the breach fault changes with the angle between the slip vector azimuth and the strike of the breach fault for a given outer fault dip if the throw-rate and strain-rate across the breach fault is the same as the outer faults assuming the outer faults have pure dip slip.

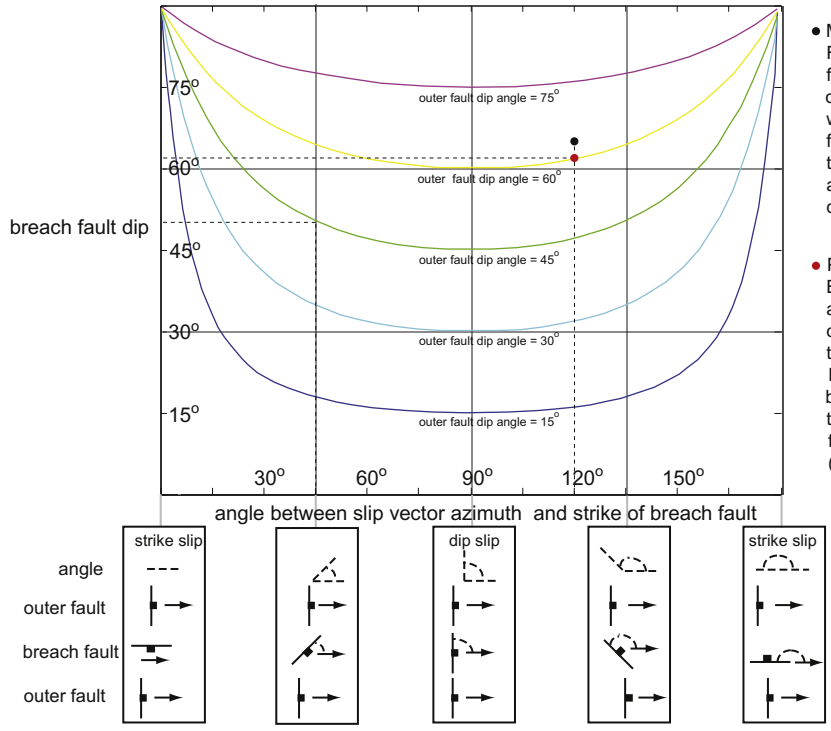

- Measured Parasano Breach Fault. Note because the breach fault plots above the line for its outer dip angle, the throw-rate will be higher across the breach fault than the outer faults and thus the deficit in total throw across the breach fault will diminish with time (fig c(iii)).
- Predicted Dip of Parasano Breach Fault if the throw-rate across it were the same as the outer faults, thus maintaining the total throw profile (fig c(i)). If the breach fault plotted below this value, the total throw deficit across the breach fault would increase with time (fig c(ii)).)

c Schematic fault maps and throw evolution where the slip vector azimuth is maintained across the relay-zone

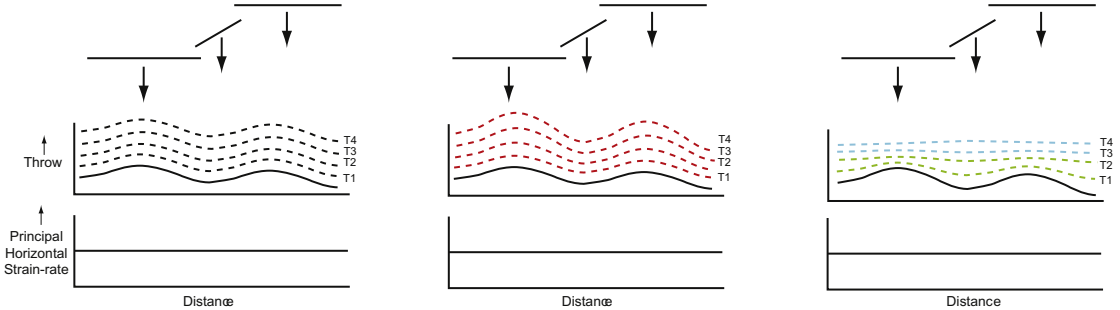

(i) If the dip of the breach fault is as the graph (b) shows for the strike of the breach fault, the throw deficit will remain the same.

(ii) If the dip of the breach fault is too low for the strike of the breach fault (see b) the throw deficit increases.

(iii) If the dip of the breach fault is too high for the strike of the breach fault (see b) the throw deficit decreases.

Deficit constant | Deficit increasing | Deficit decreasing | Deficit removed

Thus, if the principal horizontal strain-rate and the strain-rate in the direction of the slip vector remain constant, the throw-rate will increase as the dip increases:

$$T \propto \tan\vartheta \quad (3.1.10)$$

Fig. 7 shows the relationships between fault dip of an oblique breach fault, throw-rate and strain-rate graphically as ratios relative to the outer faults with a fixed dip.

3.2. Errors associated with field data

For the field example that we wish to compare with the theoretical examples in the previous section, an error of ±5% was assigned to the slip direction and plunge of the slip vector as this is the mean 99% confidence level defined statistically in stereographic projection software (Allmendinger, 1988; Roberts and Michetti, 2004; Roberts, 2007). Likewise, the error estimated for the fault strike is ±5%. The throw since 15 ± 3 ka has an uncertainty of ±20% because this is the natural variability in the throw across scarps measured in the field within a few tens of metres of a given scarp profile (Roberts and Michetti, 2004). The error in the total length of each fault is +10% as the fault tips are difficult to trace at the surface. The error propagating from the uncertainty in the location of fault tips is minimal as the post 12–18 ka throw is very small in these locations (<1–2 m) and hence the contribution to the 15 ± 3 ka strain-rate is very small. Thus, the uncertainty in location of the fault tips may cause errors where the fault extends into an area where no fault is shown. The error in the strain-rate derived from the error in the length is only relevant for grid squares at fault tips, where the strain is small in any case. Therefore, an error of 5% of the total fault length is assigned in grid boxes which contain a fault tip. Grid boxes not containing a fault tip are assigned a zero error for fault length.

4. Results

The fault system we studied can be divided into 4 or possibly 5 faults at the surface (Fig. 2). The tips of faults on this chord of the fault are interpreted to be at locations 1, 2, 3, 4, 5, 7 and 8. The throws associated with the 15 ± 3 ka scarps decreases to zero in these locations. The structure at location 6 is unclear due to poor exposure, whilst at 9, the fault is covered and thus obscured by Holocene and Pleistocene lake sediments. The map traces and topographic elevation changes reveal a relay zone between the faults between locations 1 and 2, and 5 and 6 (see Fig. 2b for numbering of faults). The fault between locations 3 and 4 has the geometry of a breaching fault that is trying to link between the two neighbouring faults. The vertical offset of the Upper Cretaceous to Eocene limestone is close to zero at location 1, reaches about 370 ± 50 m between locations 1 and 2, and decreases to about 100 m in the area adjacent to locations 3 and 4 (Fig. 5). It then increases to about 370 ± 50 m between locations 5 and 7, before approaching zero near location 9. Some uncertainty in total throw exists in some places between locations 5 and 9 (Fig. 2) due to the absence of the marker limestone. However, overall, the throw profile reveals a double maxima in throw (380 ± 50 m; 370 ± 50 m), separated by a lower throw (100 ± 50 m) across the breaching fault (Fig. 5). This throw deficit prompted us to measure the vertical offsets of 12–18 ka slopes to see how the rates of deformation varied across the relay zone.

We present 5 scarp profiles, 2 of which were first presented by Papanikolaou et al. (2005). We chose the locations of these profiles in places where there was negligible erosion or sedimentation associated with the slopes since the last glacial maximum (15 ± 3 ka). Profile (3) characterises post 12–18 ka throw for the breaching fault, whilst profiles (1), (2), (4) and (5) characterise the same for the two neighbouring faults (Figs. 2a, 4 and 5). Throw-rates were determined by dividing the vertical offset by 12 kyr and 18 kyr, to incorporate uncertainty in the exact scarp age, and thus bracket the actual deformation rate. Throw-rates for profiles (1) and (4), the positions close to total throw maxima, are 0.38 ± 0.07 mm/yr and 0.55 ± 0.11 mm/yr respectively. Errors associated with our measurements are plus/minus a few tens of centimetres on scarp profiles, so the implied error in throw-rate is negligible and smaller than our bracketed range of throw-rates due to uncertainty in the age of the slopes. With this in mind, we note that the throw-rate implied by profile (3) is 0.67 ± 0.13 mm/yr, a range of values that is large enough to be considered greater than that for profiles (1) and (4) when errors are considered. Thus, the throw-rate across the breaching fault is up to a factor of 2 higher than that for the two neighbouring faults, even though the total throw is a factor of 3–4 lower than that for neighbouring faults.

The c. 0.8 km long breaching fault dips at 67 ± 5°, and strikes obliquely (approximately 30°) to c. 2–3 km long faults outside the relay zone which dip at 61 ± 5° and 61 ± 5°. The throw/length ratios for the fault between locations 1 and 2 and 5 and 9 on Fig. 2b are c. 370/3200 and 380/3000, that is 0.12 and 0.13. If the breaching fault links these two faults, the newly linked fault will be about 6400 m in length. To gain a d/L ratio in the order of 0.1, that is self-similar with that on the precursor faults, the throw on the newly linked fault will have to increase to c. 640 m. However, the throw value at present within the zone of incipient linkage is only 100 ± 50 m. If the 12–18 kyr throw-rates within the relay zone persist, the time period needed to increase the total throw from 100 m to 640 m in the breached relay is 0.68–1.0 Myr.

To examine why throw-rates are higher in the zone of incipient linkage, horizontal strain-rate tensors were calculated for 1 × 2 km boxes (Fig. 5c–f). Strain-rates in the zone of linkage (0.169 ± 0.028 ppm/yr) are higher than those associated with the faults either side if the relay zone (0.153 ± 0.028 ppm/yr and 0.077 ± 0.019 ppm/yr). The strain-rates decrease towards the tips of the faults where the 12–18 ka throws across the scarps decrease to zero. Strain-rates along faults are commonly highest close to the centre, so the results are consistent with the outside faults and the breaching fault behaving as a single fault.

5. Discussion

The natural example we study suggests an interpretation where a throw deficit at the point of linkage between two normal faults is

Fig. 9. Diagram showing how the evolution of the total throw profile across a relay zone develops depending on the 3D orientation of the breach fault and its kinematics. (a) 3D views of a relay zone before and after breaching. (b) Graph showing how the dip of the breach fault changes with the angle between the slip vector azimuth and the strike of the breach fault for a given outer fault dip if the throw-rate and strain-rate across the breach fault is the same as the outer faults assuming the outer faults have pure dip-slip. The angle between the slip vector azimuth and the strike of the breach fault is shown schematically below the graph. (c) Schematic fault maps and schematic throw evolution where the slip vector azimuth is maintained across the relay zone. Example: assuming principal strain-rates are preserved across the relay zone and that there is only one breach fault, if the outer faults have pure dip-slip motion with a dip of 45° and the breach fault has a slip vector azimuth at 45° to the strike of the breach fault, in order to have the same throw-rate on the breach fault as the outer faults the dip on the breach fault is 50° (see dashed line Fig. 9b), in this scenario the throw deficit on the throw profile will remain (Fig. 9ci). If the breach fault dip is less than 50° the throw deficit on the throw profile will increase (Fig. 9cii). If however the dip of the breach fault is greater than 50° then the throw deficit will decrease with time (Fig. 9ciii). Also shown is where the Parasano breach fault plots on Fig. 9b; it has an outer fault dip angle of 61° and the breach fault has a slip vector azimuth at 120° to the strike of the breach fault, according to the assumptions of the model, the dip of the breach fault (67°) suggests that the total throw deficit across the breach fault will diminish with time (Fig. 9ciii).

being removed by the existence of relatively high throw-rates on a newly formed breaching fault. The total offset across the breaching fault (100 ± 50 m) is less than across the faults (370 ± 50 m; 360 ± 50 m) either side of it. The offset of Late Pleistocene–Holocene landforms and sediments show that the throw across the relay zone over the last 15 ± 3kyr (9.7 ± 1.0 m) is greater than for locations of throw maxima on the neighbouring faults (5.5 ± 0.6; 8.0 ± 0.8 m). Assuming that this is representative of the long-term rates it implies that the relay-breaching fault is younger than the outer faults; the deficit in total throw in the zone of incipient linkage exists because no throw accumulated at this point until the breaching fault became established. If the 15 ± 3 ka throw-rates persist, the deficit in total throw within the relay zone will be removed within 0.68–1.0 Myr. This is consistent with the breaching fault developing to connect the neighbouring fault segments (see fault growth Cartwright et al., 1995). The increase in horizontal strain-rate implied by the relatively high throw-rates on the relay-breaching fault after linkage must be explained as we have no reason to postulate that regional strain-rates have increased.

We explain the above by pointing out that the horizontal strain across a fault, its throw, its kinematics and its strike and dip are interlinked variables (Figs. 6 and 7). For example, Fig. 9 shows that to maintain a constant horizontal principal strain-rate across a relay zone the dip of the breach fault, the dip of the faults outside of the relay zone, the 3D orientation of the slip vector azimuth, the strike of the breach fault and the throw-rate are inter-related. Specifically, if the outer faults are dip-slip, and the slip vector azimuth on the breach fault is parallel to that on the outer faults, as is the case for the Parasano fault, the principal horizontal strain-rate can only be constant along strike for the case where a throw deficit is being removed in the relay zone if the dip of the breaching fault is steeper than predicted by the graph in Fig. 9b. This may explain why the throw deficit is being removed on the Parasano breach fault; the fault has, for some reason, developed with a dip that is steeper than anticipated by the graph in Fig. 9b.

To explain the relationship between strain-rates, fault geometries and fault kinematics in more detail, we state the following. Assuming that the outer faults are dip-slip, and that the horizontal principal strain-rate is constant along strike:

(1) If the 3D orientation of the breach fault matches that of the graph in Fig. 9b then the throw profile shape, i.e. multiple maxima, will be preserved with the deficit neither increasing or decreasing (Fig. 9c(i)).
(2) If the dip of the breach fault is lower than that on Fig. 9b then the throw-rate on the breach fault will be lower than on the outer faults and hence the throw deficit on the total throw profile across the relay zone will increase with time (Fig. 9c(ii)). A specific example of this scenario is if the breach fault is oblique in terms of strike to the outer faults, but has the same dip as them.
(3) If the dip of the breach fault is higher than on Fig. 9b, the throw-rate across the breach fault will be greater than on the outer faults; the deficit in the total throw profile across the relay zone will decrease with time (Fig. 9c(iii)). A specific example of this is the Parasano breach fault, where the plunge of the slip vector is the same ($\pm 5^\circ$) along the oblique breach fault as on the outer faults (Fig. 2). For this to occur the dip of the breach fault must be greater than on the outer faults (Eq. (3.1.7)) and this is the case as shown by the poles to the fault planes (Fig. 2); the mean dip measured on striated fault planes for the breaching fault is $67 \pm 5^\circ$, with those for the surrounding faults being $61 \pm 5^\circ$, where the error is one standard deviation; average dips for the free faces on the scarp profiles are 65° for the breaching fault and 61° for the surrounding faults. Note that lower values for the dip of the oblique fault will mean that a greater proportion of the displacement contributes to the heave, providing higher values for the horizontal extensional strain for a given value of fault strike obliquity.

In summary, if the horizontal strain-rate is conserved across a relay zone then the 3D orientation of the breach fault relative to the outer faults will determine whether a double peak throw maxima is preserved.

To examine whether the example we describe above from the Parasano fault is typical, we have reviewed the literature of the dips of breach faults. Examples of breaching faults with both steeper dips than surrounding faults and shallower dips than surrounding faults are present within the literature. For example (1) (Roberts, 2007; his Fig. 7) shows the South Alkyonides Fault in central Greece, where the breach faults are steeper and the slip vector azimuth is maintained; (2) (Morewood and Roberts, 2000, their Fig. 2 VMF, Locality 6) shows the Velino Fault in central Italy where the breach fault is shallower (see following discussion of the slip vector); and (3) (Taylor et al., 2004, their Fig. 7) shows the Rangitaiki Fault, New Zealand, where the R2 relay fault has a shallower dip than the R1 and R3 segments it connects. Thus, the Parasano fault example is not atypical of breaching faults as examples exist where the breach fault can be steeper or shallower than the surrounding faults.

Note so far we have discussed the case of a breaching fault with the same slip vector azimuth as the outer faults that it connects; in other words, the slip vector azimuth on the breaching fault is controlled by the regional extension direction. However, examples exist in the literature where the slip vector azimuth in a relay zone is not the same as that on the outer faults. The WNW-ESE striking Velino fault (Fig. 2) has a slip vector azimuth towards the SSW, producing local dip-slip kinematics, whereas the NW-SE striking outer Fucino and Fiamignano faults, although displaying converging patterns of slip, are overall dip-slip faults with extension to the SW (Roberts and Michetti, 2004); the WSW-ENE striking Tre Monti fault neighbouring the Velino fault is also a breach fault and also shows dip-slip kinematics so that the slip vector azimuth is towards the SSE (Fig. 2). We are unsure of exactly why slip vector azimuths oblique to the regional extension direction can develop in relay zones. We suspect that the Velino and Tre Monti faults are accommodating extension along the strike of the fault system. Specifically, extension caused by development of the hanging-wall basin to the Fucino fault causes a component of along strike extension (release faults sensu Destro, 1995; see Morewood and Roberts, 2000); the Velino and Tre Monti faults are working together with the Fucino fault to maintain constant strain-rates along the strike of the relay zone (see Faure Walker et al., submitted for publication). We have not studied in detail whether the steeply dipping Tre Monti or the shallowly dipping Velino Fault dominates the strain, or if strain is shared between the faults which have different dips (Velino Fault dip $46^\circ \pm 9^\circ$; Tre Monti Fault dip $73^\circ \pm 6^\circ$). However, here we simply wish to point out the existence of structures that are different to the Parasano example described in this paper; whether the throw profile is maintained across the Velino and Tre Monti examples needs further study.

The above shows that the strain across a fault depends on the 3D orientation of the fault and its kinematics within a regional strain-rate field. To determine the history of throw accumulation it is clear that one must know how strain is accommodated and hence the geometry, kinematics and rates of slip on every fault within a relay zone should be known. We note that such a study involving knowledge of the dip of breaching faults within relay zones and their kinematics will be difficult if examples are in the sub-surface and are imaged only by seismic reflection data.

The wider implications of the above findings are twofold:

(1) Strain-rates across active normal faults control the geomorphic evolution of the footwall topography and the sedimentary and stratigraphic patterns that develop in hanging-wall basins (Cowie et al., 2006). The base level for rivers draining the footwall is controlled by the relative uplift rate across the fault, which depends on the vertical component of the strain-rate, i.e., the fault throw-rate, as well as the rate of sedimentation in the hanging-wall. High relative uplift rates favour steeper, narrower river channels and higher rates of hill-slope erosion with an increased likelihood for land-sliding. In contrast, low relative uplift rates may be accommodated mainly by variations in channel width (Whittaker et al., 2007) with only subtle increases in channel and hill-slope gradients (e.g. Cowie et al., 2008). The results of the present study predict that relay zone catchments may exhibit different geomorphologies, and produce different sediment volumes and calibre, depending on the dip angle and strike of the breaching fault, as this fundamentally controls the relative uplift rate where the drainage enters the hanging-wall basin.

(2) Strain-rates across active faults control seismic hazard because earthquake recurrence intervals for a given earthquake magnitude are shorter for faults that are accommodating more rapid deformation. This paper highlights the fact that care must be taken when using the total throw across a fault as a proxy for fault activity rates. For example, a deficit in total throw at a point of fault linkage is not necessarily a point of low horizontal strain-rate as this depends on the strike and dip of the breaching fault for a given slip vector. Breached relays with low-dip breach faults will preserve pre-linkage throw deficits and may then be erroneously interpreted as persistent boundaries to earthquake slip, when in fact relatively high horizontal strain-rates and relatively short recurrence intervals for a given earthquake magnitude will be accumulating at the point of linkage.

6. Conclusion

Rates of throw accumulation and total throws for an active normal fault in the Italian Apennines reveal that throw-rates are higher within a zone of incipient fault linkage compared to that for the two neighbouring faults, even though total throws on the neighbouring faults are a factor of 3–4 times greater than that for a breaching fault growing in the zone of incipient linkage. This pattern of throw-rates will remove a deficit in total throw at the site of a former en echelon relay zone. This occurs because the breaching fault is in the middle of the newly linking fault and there is a positive correlation between the angle of obliquity of the strike of a fault and the throw-rate needed to maintain strain-rates for a given kinematic slip-vector. The opposite situation, where the throw deficit is preserved, will characterise examples where the dip of newly formed breaching fault has a relatively low value. Thus, whether the breach fault develops a dip that is steeper or shallower than that on the neighbouring precursor faults will influence the subsequent rate of throw accumulation and hence the landscape evolution and seismic hazard interpretation associated with that structure.

Acknowledgements

The work was funded by NERC GR9/02995, NERC NE/B504165/1, NER/S/A/2006/ 14042, NE/E01545X/1 and Birkbeck, University of London. We thank Andy Nicol and Jonathan Bull for their reviews which helped improve the manuscript.

References

Allmendinger, R.W., 1988–2005. Stereonet v6.3 X (Carbon) Academic Version.
Anderson, H., Jackson, J., 1987. Active tectonics of the Adriatic region. Geophysical Journal International 91 (3), 937–983.
Bull, J.M., Barnes, P.M., Lamarche, G., Sanderson, D.J., Cowie, P.A., Taylor, S.K., Dix, J.K., 2006. High-resolution record of displacement accumulation on an active normal fault: implications for models of slip accumulation during repeated earthquakes. Journal of Structural Geology 28, 1146–1166.
Cartwright, J.A., Trudgill, B.D., Mansfield, C.S., 1995. Fault growth by segment linkage: an explanation for scatter in maximum displacement and trace length data from the Canyonlands Grabens of SE Utah. Journal of Structural Geology 17, 1319–1326.
Cavinato, G.P., Carusi, C., Dall'Asta, M., Miccadei, E., Piacentini, T., 2002. Sedimentary and tectonic evolution of Plio-Pleistocene alluvial and lacustrine deposits of Fucino Basin (central Italy). Sedimentary Geology 148, 29–59.
Cowie, P.A., 1998. A healing-reloading feedback control on the growth rate of seismogenic faults. Journal of Structural Geology 20 (8), 1075–1087.
Cowie, P.A., Roberts, G.P., 2001. Constraining slip rates and spacings for active normal faults. Journal of Structural Geology 23, 1901–1915.
Cowie, P.A., Underhill, J.R., Behn, M.D., Lin, J., Gill, C., 2005. Spatio-temporal evolution of strain accumulation derived from multi-scale observations of Late Jurassic rifting in the northern North Sea: a critical evaluation of models for lithospheric extension. Earth and Planetary Science Letters 234, 401–419.
Cowie, P.A., Attal, M., Tucker, G.E., Whittaker, A.C., Naylor, M., Ganas, A., Roberts, G.P., 2006. Investigating the surface process response to fault interaction and linkage using a numerical modelling approach. Basin Research 18 (3), 231–266.
Cowie, P.A., Whittaker, A.C., Attal, M., Roberts, G.P., Tucker, G.E., Ganas, A., 2008. New constraints on sediment flux dependent river incision: implications for extracting tectonic signals from river profiles. Geology 36 (7), 535–538.
Dawers, N.H., Anders, M.H., 1995. Displacement-length scaling and fault linkage. Journal of Structural Geology 17, 607–614.
Destro, N., 1995. A variety of cross fault in linked extensional fault systems, in the Sergipe-Alagoas Basin, NE Brazil. Journal of Structural Geology 17, 615–629.
Doglioni, C., 1993. Some remarks on the origin of foredeeps. Tectonophys 228, 1–20.
England, P., Molnar, P., 1997. The field of crustal velocity in Asia calculated from Quaternary rates of slip on faults. Geophysics Journal International 130, 551–582.
Faure Walker, J., Roberts, G.P., Sammonds, P., Cowie P., 2009. Comparison of earthquake strains over 10^2 and 10^4 year timescales: insights into variability in the seismic cycle in the central Apennines, Italy. Journal of Geophysical Research, submitted for publication.
Fung, Y.C., 1977. A First Course in Continuum Mechanics. Prentice-Hall, Inc., Englewood Cliffs, NJ.
Giraudi, C., Frezzotti, M., 1997. Late Pleistocene glacial events in the central Apennines, Italy. Quaternary Research 48, 280–290.
Gupta, A., Scholz, C.H., 2000. A model of normal fault interaction based on observations and theory. Journal of Structural Geology 22, 865–879.
Haines, A.J., Holt, W.E., 1993. A procedure for obtaining the complete horizontal motions within zones of distributed deformation from the inversion of strain-rate data. Journal of Geophysical Research 98 (B7), 12057–12082.
Holt, W.E., Haines, A.J., 1995. The kinematics of northern South Island, New Zealand, determined from geologic strain rates. Journal of Geophysical Research 100 (B9), 17991–18010.
Jackson, C.A.L., Gawthorpe, R.L., Sharp, I.R., 2002. Growth and linkage of the East Tanka fault zone, Suez rift: structural style and syn-rift stratigraphic response. Journal of the Geological Society London 159, 175–187.
Jolivet, L., Facenna, C., Goffe, B., Mattei, M., Rosseti, F., Brunet, C., Storti, F., Funiciello, R., Cadet, J.P., d'Agostino, N., Parra, T., 1998. Midcrustal shear zones in postorogenic extension: example from the northern Tyrrhenian Sea. Journal of Geophysical Research 103 (B6), 12123–12160.
Kostrov, V.V., 1974. Seismic moment and energy of earthquakes, and seismic flow of rock. Izv. Earth Physics 1 (23–40), 13–21. translation UDC 550.341.
Main, I.G., 1996. Statistical physics, seismogenesis, and seismic hazard. Reviews of Geophysics 34 (4), 433–462.
Margottini, C., Screpanti, A., 1988. Temporal evolution of the seismic crisis related to the 13th January 1915, Avezzano earthquake. In: Margottini, C., Serva, L. (Eds.), Historical Seismicity of Central-eastern Mediterranean Region. Proceedings of the 1987 ENEA-IAEA International Workshop. ENEA, Rome, pp. 185–193.
McLeod, A., Dawers, N.H., Underhill, J.R., 2000. The propagation and linkage of normal faults: insights from the Strathspey-Brent-Statfjord fault array, northern North Sea. Basin Research 12, 263–284.
Michetti, A.M., Ferreli, L., Esposito, E., Porfido, S., Blumetti, A.M., Vittori, E., Serva, L., Roberts, G.P., 2000. Ground Effects during the 9 September 1998, Mw = 5.6, Lauria Earthquake and the seismic potential of the aseismic Pollino Region in Southern Italy. Seismological Research Letters 71, 31–46.
Molnar, P., 1983. Average regional strain due to slip on numerous faults of different orientations. Journal of Geophysical Research 88, 6430–6432.

Morewood, N.C., Roberts, G.P., 2000. The geometry, kinematics and rates of deformation within an en echelon normal fault boundary, central Italy. Journal of Structural Geology 22, 1027–1047.
Nicol, A., Walsh, J.J., Watterson, J., Underhill, J.R., 1997. Displacement rates of normal faults. Nature 390, 157–159.
Nicol, A., Walsh, J., Berryman, K., Villamor, P., 2006. Interdependence of fault displacement rates and paleoearthquakes in an active rift. Geology 34, 865–868.
Palumbo, L., Benedetti, L., Bourles, D., Cinque, A., Finkel, R., 2004. Slip history of the Magnola fault (Apennines, Central Italy) from ^{36}Cl surface exposure dating: evidence for strong earthquakes over the Holocene. Earth and Planetary Science Letters 225, 163–176.
Papanikolaou, I.D., Roberts, G.P., Michetti, A.M., 2005. Fault scarps and deformation rates in Lazio-Abruzzo, Central Italy: comparison between geological fault slip-rate and GPS data. Tectonophysics 408, 147–176.
Patacca, E., Sartori, R., Scandone, P., 1990. Tyrrhenian Basin and Apenninic Arcs: kinematic relations since late Tortonian times. Memorie della Società Geologien d'Italia 45, 425–451.
Peacock, D.C.P., 2003. Scaling of transfer zones in the British Isles. Journal of Structural Geology 25 (10), 1561–1567.
Peacock, D.C.P., Sanderson, D.J., 1991. Displacements, segment linkage and relay ramps in normal fault zones. Journal of Structural Geology 13 (6), 721–733.
Roberts, G.P., 2006. Multi seismic cycle velocity and strain fields for an active normal fault system, central Italy. Earth and Planetary Science Letters 251, 44–51.
Roberts, G.P., 2007. Fault orientation variations along the strike of active normal fault systems in Italy and Greece: implications for predicting the orientations of subseismic-resolution faults in hydrocarbon reservoirs. AAPG Bulletin 91 (1), 1–20.
Roberts, G.P., Michetti, A.M., 2004. Spatial and temporal variations in growth rates along active normal fault systems: an example from the Lazio-Abruzzo Apennines, central Italy. Journal of Structural Geology 26, 339–376.
Roberts, G.P., Cowie, P., Papanikolaou, I., Michetti, A.M., 2004. Fault scaling relationships, deformation rates and seismic hazards: an example from the Lazio-Abruzzo Apennines, central Italy. Journal of Structural Geology 26, 377–398.
Taylor, S.K., Bull, J.M., Lamarche, G., Barnes, P.M., 2004. Normal fault growth and linkage during the last 1.3 million years: an example from the Whakatane Graben, New Zealand. Journal of Geophysical Research 109, B02408. doi:10.1029/2003JB002412.
Vezzani, L., Ghisetti, F., 1998. Carta Geologica Dell'Abruzzo, SELCA, Via R. Giuliani, 153, Firenze, 1:100,000.
Walsh, J.J., Watterson, J., Childs, C., Nicol, A., 1996. Ductile strain effects in the analysis of seismic interpretations of normal fault systems. In: Buchanan, P.G. (Ed.), Modern Developments in Structural Interpretation, Validation and Modelling. Geological Society, London, Special Publications, vol.99, pp.27–40.
Walsh, J.J., Watterson, J., Bailey, W.R., Childs, C., 1999. Fault relays, bends and branch-lines. Journal of Structural Geology 21 (8–9), 1019–1026.
Walsh, J.J., Childs, C., Imber, J., Manzocchi, T., Watterson, J., Nell, P.A.R., 2003a. Strain localisation and population changes during fault system growth within the Inner Moray Firth, Northern North Sea. Journal of Structural Geology 25, 307–315.
Walsh, J.J., Bailey, W.R., Childs, C., Nicol, A., Bonson, C.G., 2003b. Formation of segmented normal faults: a 3-D perspective. Journal of Structural Geology 25 (8), 1251–1262.
Whittaker, A.C., Cowie, P.A., Attal, M., Tucker, G.E., Roberts, G.P., 2007. Contrasting transient and steady state rivers crossing active normal faults: new field observations from Italy. Basin Research 19, 529–556.